ACS APPLIED MATERIALS & INTERFACES

Research Article

Cite This: ACS Appl. Mater. Interfaces 2019, 11, 29522−29535

www.acsami.org

Meso-Cellular Silicate Foam-Modified Reduced Graphene Oxide with a Sandwich Structure for Enzymatic Immobilization and Bioelectrocatalysis

Huiting Wang,[†] Fei Teng,[†] Ling Zhang,[‡,§] Qian Zhang,*[,†,§] Hairan Zhang,[†] Tingting Pei,[†] Shun Li,[†] and Lixin Xia*[,†]

[†]College of Chemistry, Liaoning University, Shenyang 110036, China

[‡]College of Chemistry and Chemical Engineering, Shenyang Normal University, Shenyang 110034, China

[§]Key Laboratory of Functional Inorganic Material Chemistry, Ministry of Education of the People's Republic of China, Heilongjiang University, Harbin 150080, China

Supporting Information

ABSTRACT: An integrated composite of meso-cellular silicate foam (MCF)-modified reduced graphene oxide (MCF@rGO) was designed and synthesized based on polyethylene oxide−polypropylene oxide−polyethylene oxide (P123)-modified rGO (P123-rGO). As the polymeric template for the fabrication of mesoporous silicates, modified P123 greatly improved the affinity between the nanosheet and the in situ formed MCFs, resulting in the formation of thin layers of MCFs on both sides of rGO. Therefore, the MCFs@rGO formed exhibited a unique sandwich structure with an inner skeleton of rGO and two outer layers of MCFs. The outer modification by MCFs, with the presence of large mesopores, not only shifted the surface property of rGO from hydrophobic to hydrophilic but also offered immobilized enzymes a favorable microenvironment to maintain their bioactivity. Meanwhile, the inner skeleton of rGO compensated for the weak conductivity of MCFs, providing a pathway for the direct electron transfer (DET) of various redox enzymes or proteins, such as hemoglobin (Hb), horseradish peroxidase, glucose oxidase (GOD), and cholesterol oxidase. It was found that the DET signal obtained from Hb-MCFs@rGO/glassy carbon electrode (GCE) was much larger than the sum of the signals from two components-based modified electrodes of Hb-P123-rGO/GCE and Hb-MCFs/GCE. A similar improvement in DET signal was also observed using GOD-MCFs@rGO/GCE. The significant enhancement of DET signals for both protein electrodes can be ascribed to the synergistic effects generated from the integration of the two components, one of which enhances biocompatibility and the other enhances conductivity. The bioelectrocatalytic performance of Hb and GOD electrodes was further investigated. As for Hb-MCFs@rGO/GCE, the GOD electrode displayed excellent analytical performance for the detection of hydrogen peroxide (H_2O_2), including a good sensitivity of 0.25 μA μmol^{-1} L cm^{-2}, a low detection limit of 63.6 nmol L^{-1} based on S/N = 3, and a low apparent Michaelis−Menten constant (K_M^{app}) of 49.05 μmol L^{-1}. GOD-MCFs@rGO/GCE also exhibited good analytical performance for the detection of glucose, with a wide linear range of 0.25−8.0 mmol L^{-1}. In addition, blood glucose detection in samples of human serum was successfully achieved using GOD-MCFs@rGO/GCE with a low quantification limit.

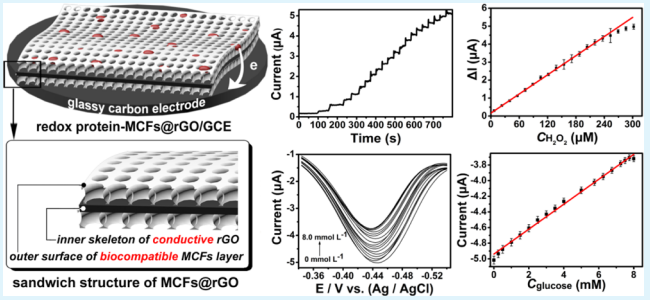

KEYWORDS: *meso-cellular silicate foam, reduced graphene oxide, enzymatic immobilization, bioelectrocatalysis, electrochemical biosensor*

1. INTRODUCTION

Direct electron transfer (DET) of redox enzymes or proteins has attracted significant research attention because of its application in various fields of bioscience. The investigation of DET is not only conducive to understanding the metabolic processes in biological systems, but it also has promising applications to the fabrication of mediator-free electrochemical biosensors.[1−6] However, the DET of redox enzymes is not easily achieved, owing to the fact that the redox center of these enzymes is generally buried deep in complex peptide chain structures.[7−9] Moreover, the inactivity of immobilized enzymes, caused by the hydrophobic electrode surface, greatly hampers DET.[10,11] Thus, it is necessary to design and synthesize a suitable electrode material with both conductivity and biocompatibility, which can provide both a favorable microenvironment and a pathway for the electron transfer of

Received: May 16, 2019
Accepted: July 26, 2019
Published: July 26, 2019

DOI: 10.1021/acsami.9b08569
ACS Appl. Mater. Interfaces 2019, 11, 29522−29535

redox enzymes in order to achieve quicker DET between immobilized hemoglobin (Hb) and the surface of the electrode. Various electrode materials composed of multiple components with both conductivity and biocompatibility have been designed and synthesized for the construction of biosensors, resulting in excellent performance. Research suggests that the amplification of the DET signal can be successfully achieved with enzymatic electrodes modified with integrated hybrids, especially those composed of carbon nanomaterials and biocompatible modifiers.[12−14]

Graphene is a typical two-dimensional (2D) nanomaterial with unique properties and structure.[15,16] Because of their inherent conductivity and large surface area, carbonous nanomaterials have attracted great interest in the field of bioelectrochemistry.[17] Despite their merits, graphene-based materials still exhibit some shortcomings, which limit their application in the construction of enzymatic biosensors. For instance, conductive graphene-based materials, such as reduced graphene oxide (rGO), tend to be hydrophobic because of their inherent conjugated structures.[18,19] However, the bioactivities of redox enzymes are greatly reduced if they are directly adsorbed onto such a hydrophobic carbonous surface, thus further influencing their behavior in DET.[20,21] Therefore, to improve the affinity between enzymes and electrodes, it is highly desirable to modify rGO with a biocompatible component in order to convert its hydrophobic surface to a hydrophilic one.[22−24]

As a type of biocompatible material, mesoporous silicates have attracted considerable attention in recent years because of their application in the field of enzymatic immobilization.[24] A recent report suggested that as compared to mesoporous silicates with conventional mesopores, the bioactivity of immobilized enzymes can be enhanced after their entrapment into large-sized mesopores, such as those found in mesoporous cellular silicate foams (MCFs).[25] Thus, it appears that mass transfer within mesoporous silicates can be improved in the presence of large mesopores, which is conducive to the enhancement of the analytical performance of a biosensor. However, although MCFs act as a biocompatible host matrix for enzymatic immobilization, their weak conductivity greatly hampers the electron transfer of entrapped enzymes.[26] In other words, MCFs do not exhibit conductivity similar to rGO. Owing to the inherently poor conductivity of MCFs, the as-formed modified electrodes often exhibit a weak DET signal from the immobilized redox enzymes, thus leading to inferior analytical performance, as compared to other types of electrochemical biosensors.[27] Therefore, if the modifying MCFs could be combined with rGO to form an integrated composite of MCFs@rGO, the as-prepared material should exhibit both biocompatibility and conductivity. On one hand, outer modification by MCFs can convert the hydrophobic surface of rGO to a hydrophilic surface, providing the immobilized enzymes with a biocompatible microenvironment. On the other hand, the inner backbone of rGO can greatly compensate for the poor electron transportability of MCFs, thus offering an efficient conductive pathway to facilitate DET between the entrapped enzymes and the surface of the electrode. Moreover, because of the open structure and large surface area of both MCFs and rGO, the entrapped enzymes or proteins can be fully exposed to the electrolyte, thus greatly facilitating their bioelectrocatalysis. In brief, it appears that an integrated composite of MCFs@rGO may act as an excellent matrix for immobilized proteins to achieve enhanced DET. To date, integrated hybrids composed of a 2D graphene skeleton and various modifiers have already been utilized as electrode materials in the field of electrochemistry to construct high-performance batteries or capacitors.[28−30] However, MCF@rGO materials with excellent conductivity and biocompatibility have not yet been introduced for enzymatic immobilization and bioelectrocatalysis.

In this work, a novel MCF@rGO composite with a sandwich structure was developed via the in situ growth of MCFs on the surface of polyethylene oxide−polypropylene oxide−polyethylene oxide (P123)-modified rGO (P123-rGO). Such a unique structure endowed the composite with hydrophilicity, open structure, and conductivity.[13,31] It was found that various immobilized proteins or enzymes with different types of redox centers, whether flavin adenine dinucleotide (FAD) or heme, preserved their own native structures and bioactivities, achieving quicker DET between themselves and the surface of the glassy carbon electrode (GCE). Owing to the enhanced DET, the two prepared modified electrodes, Hb-MCFs@rGO/GCE and glucose oxidase (GOD)-MCFs@rGO/GCE, exhibited excellent performance of bioelectrocatalysis toward the detection of H_2O_2 and glucose, respectively. Moreover, GOD-MCFs@rGO/GCE could be applied to the detection of glucose in human blood serum samples, with a low quantification limit. GOD-MCFs@rGO/GCE also showed excellent thermal stability because of the biocompatible microenvironment of immobilized GOD provided by the mesopores of the MCF outer layers.

2. EXPERIMENTAL METHODS

2.1. Materials and Instruments. Polyethylene oxide−polypropylene oxide−polyethylene oxide (P123) was purchased from Sigma. 1,3,5-Trimethylbenzene (TMB), tetraethyl orthosilicate (TEOS), and other chemicals were purchased from Sinopharm Chemical Reagent Co. Ltd. (Shanghai, China). All aqueous solutions were freshly prepared using Milli-Q purified water (>18 MΩ cm^{-1}). Samples of human serum were obtained from the Affiliated Hospital of Liaoning University.

2.2. Preparation of P123-rGO. Graphene oxide (GO) was first synthesized according to the modified Hummers method.[32] For the preparation of P123-modified rGO (P123-rGO), 12.5 mg of GO powder was first added to 10 mL of deionized water, and a homogeneous dispersion was formed by ultrasonic treatment for 30 min. Next, 0.5 g of P123 and 10 mL of ammonia were added to the dispersion, which was then stirred for 30 min. The mixture obtained after the addition of 2.5 mL of hydrazine hydrate was then refluxed for 24 h. After the black dispersion was cooled to room temperature, the mixture was multicentrifuged and washed with water to neutral pH. The P123-rGO obtained was dried for 12 h at 50 °C.

2.3. Preparation of MCFs@rGO. In order to synthesize MCFs@rGO, 1.0 g of P123 was first dissolved into 8.0 mL of HCl (4.5 mol L^{-1}) with stirring. This solution was then mixed with 50 mL of the P123-rGO dispersion containing 0.72 g of TMB. After 1.41 g of TEOS was added into the merged dispersion, the mixture was stirred for 20 h at 38 °C. Afterward, the gray dispersion was transferred into a hydrothermal reactor and heated at 110 °C for 24 h. The resulting gray dispersion was filtered and washed with 30 mL of toluene and acetone, respectively, after cooling to room temperature. The prepared MCFs@rGO was then calcined at 500 °C in a nitrogen atmosphere for 1 h to remove the template of P123.

2.4. Preparation of Various Modified Electrodes. Prior to modification, a bare GCE with a diameter of 3.0 mm was polished to a mirror finish using a piece of polishing cloth, with 1.0, 0.3, and 0.05 μm of alumina powder in turn. The electrode was then rinsed thoroughly with deionized water and sonicated in acetone, ethanol, and deionized water. The clean electrode was dried under a high-

DOI: 10.1021/acsami.9b08569
ACS Appl. Mater. Interfaces 2019, 11, 29522−29535

Scheme 1. Fabrication of the MCF@rGO Composite for the Achievement of DET between Immobilized Redox Protein or Enzyme and GCE

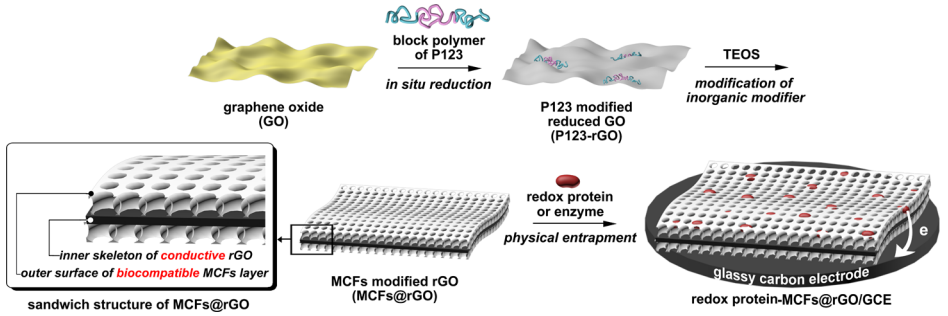

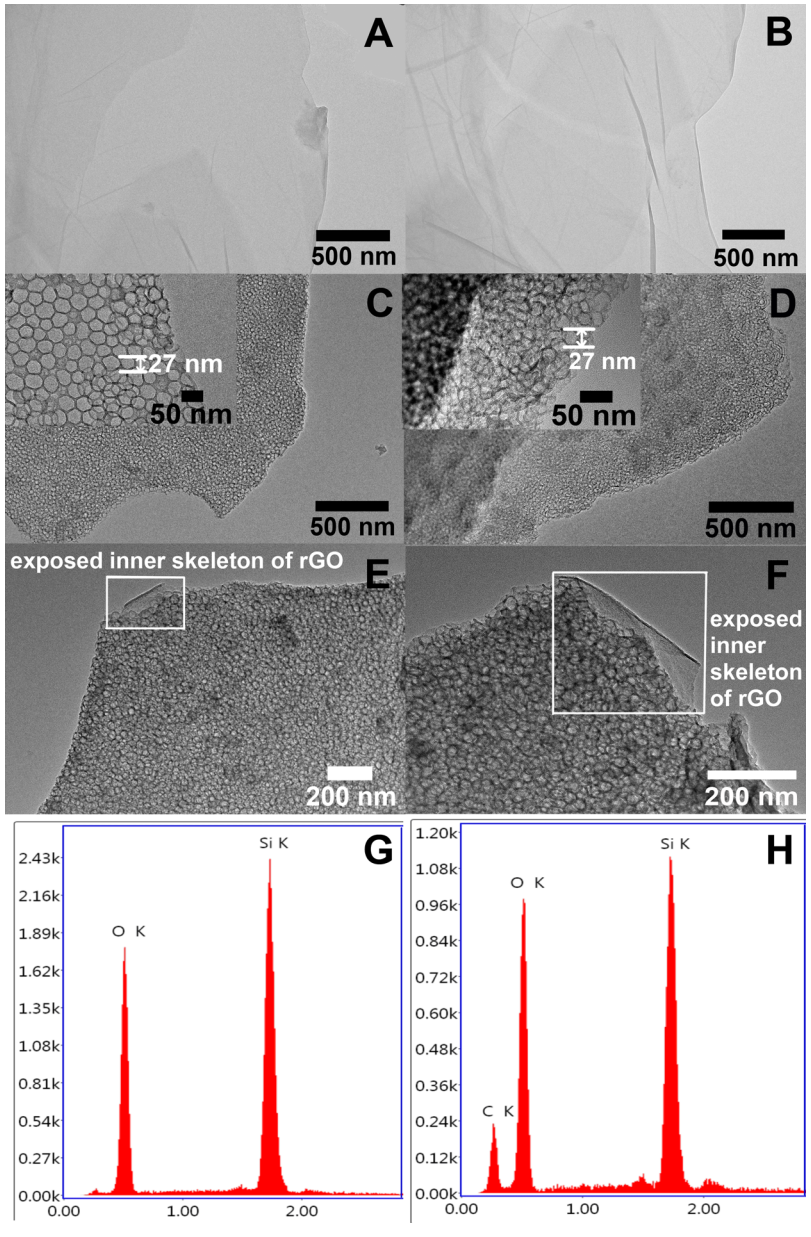

Figure 1. TEM images of GO (A), P123-rGO (B), MCFs@rGO (C,E,F) and enlarged TEM image of MCFs@rGO (inset of C), MCFs (D) and enlarged TEM image of MCFs (inset of D). EDS of MCFs (G) and MCFs@rGO (H).

purity nitrogen atmosphere. The modified electrodes were prepared using a simple casting method. Taking Hb-MCFs@rGO/GCE as an example, 0.25 mL of solution containing 2.5 mg of Hb was merged with the dispersion of 1.0 mg of MCFs@rGO in 0.50 mL of deionized water. The mixture was stirred for 20 min and stored at 4 °C for 24 h. After the addition of 0.25 mL of 5% Nafion solution to the mixture,

DOI: 10.1021/acsami.9b08569
ACS Appl. Mater. Interfaces 2019, 11, 29522−29535

the final dispersion was stirred for another 10 min. Then, 6.0 μL of the above dispersion was dropped onto the pretreated GCEs in order to fabricate the corresponding modified Hb-MCFs@rGO/GCE. After that, the prepared electrodes were covered with a beaker to allow the excess water to evaporate slowly at 4 °C. Other modified electrodes, including rGO/GCE, MCFs/GCE, MCFs@rGO/GCE, Hb-MCFs/GCE, Hb-P123-rGO/GCE, GOD-MCFs/GCE, GOD-P123-rGO/GCE, horseradish peroxidase (HRP)-MCFs@rGO/GCE, GOD-MCFs@rGO/GCE, and cholesterol oxidase (ChOx)-MCFs@rGO/GCE were also prepared using the method described above.

2.5. Characterization. Transmission electron microscopy (TEM) images were obtained with a 2100 transmission electron microscope (JEOL Hitachi, Japan) at an accelerating voltage of 100 kV. Scanning electron microscopy (SEM) analyses and energy-dispersive spectroscopy (EDS) analyses were implemented with a scanning electron microscope (JEOL JSM-7400F) equipped with an energy-dispersive spectrometer, operating at 5 kV. Powder X-ray diffraction (XRD) measurements of rGO and MCFs@rGO were obtained with a D8 9 ADVANCE X-ray powder diffractometer (Bruker, Germany) using a Cu Kα radiation source (λ = 0.154056 nm for Kα_1) working at 40 kV and 40 mA. The powder samples were ground to 320 mesh and placed in cuvettes. Each measurement was scanned at a rate of 10° per minute, with a range of 5−60°. UV−vis spectra of GO, P123-rGO, MCFs@rGO, Hb, and Hb-MCFs@rGO-based aqueous dispersions were measured over a wavelength range of 200−700 nm using an L35 UV−vis spectrophotometer (PerkinElmer, America). Fourier transform IR (FTIR) spectra of GO, P123-rGO, MCFs@rGO, MCFs, Hb, and Hb-MCFs@rGO were collected in a transmission mode in a PE-FT spectrophotometer (PerkinElmer, America) using a thin KBr disk as the mounting medium of the samples. Raman spectra were measured on an inVia Raman spectrometer (Renishaw Trading Co., Ltd.). The samples of GO, rGO, P123-rGO, and MCFs@rGO were scanned 3 times for 10 s each time at a wavelength of 532 nm and a laser power of 2.5 mW. The contact angle test was measured with a sample that was pressed into thin slices at room temperature. The dynamic light scattering (DLS) measurement was obtained by Zetasizer Nano (Malvern, Britain). Electrochemical measurements, such as electrochemical impedance spectroscopy (EIS), cyclic voltammetry (CV), and differential pulse voltammetry (DPV), were obtained with a CHI660e electrochemical workstation (Shanghai Chenhua Instruments, China). EISs were measured in 10.0 mmol L^{-1} $Fe(CN)_6^{4-/3-}$ (1:1) solution containing 0.10 mol L^{-1} KCl, with a frequency range of 0.1 to 10^5 Hz, an open-circuit potential of 0.2 V, and an amplitude of 5 mV. Phosphate-buffered saline (PBS, 0.1 mol L^{-1}) solutions with pH values of 7.0 and 7.4, respectively, were used as the electrolyte solutions. The PBS solutions were purged with highly purified nitrogen or air for at least 30 min to obtain nitrogen- or air-saturated atmospheres before the electrochemical analysis of CV or DPV.

3. RESULTS AND DISCUSSION

3.1. Preparation and Characterization of MCFs@rGO. Scheme 1 depicts the idealized scheme for the preparation of MCFs@rGO with a sandwich structure for the immobilization and bioelectrocatalysis of redox proteins or enzymes. As shown, P123-rGO was first synthesized via the in situ reduction of GO with a block polymer of P123. The modification of P123 on rGO forms an efficient barrier around the nanosheet, preventing irreversible aggregation. The prevention of aggregation between graphene layers is an important prerequisite for the formation of MCFs@rGO with a uniform structure and desired electrochemical properties. More importantly, as a polymeric template for the formation of mesoporous silicates, the modifier P123 also established an efficient linkage between rGO and MCFs. The modified P123 greatly improved the affinity between the nanosheet and the in situ formed MCFs, resulting in the formation of thin layers of MCFs on both sides of rGO. Therefore, the as-formed integrated composite of MCFs@rGO exhibited a unique sandwich structure. The outer sphere was a biocompatible MCF layer that exhibited large mesopores for protein immobilization. The inner core was a nanosheet of rGO that served as a skeleton for the composite. Meanwhile, this nanosheet also acted as a conductive framework for the electron transfer of entrapped enzymes. As a result, the immobilized enzyme with favorable orientation could not only achieve DET with the electrode but also exhibited excellent bioelectrocatalytic performance because of the open structure of MCFs@rGO.

Figure 1A shows the typical morphology of GO. As shown, GO exhibits a nanosheet with a 2D wrinkled surface of about 10 μm in size. As can be observed in Figure 1B, the subsequently formed P123-rGO maintained the original 2D sheetlike morphology after in situ reduction and modification. It is known that the inherent electron transport nature of rGO is highly dependent on the number of layers. It has been reported that graphene with less than 10 layers generally exhibits excellent electron transport properties compared to graphene with a single layer.[33] Because the rGO inner skeleton of MCFs@rGO was designed to promote the transfer of electrons during the process of bioelectrocatalysis, it is very important that the monolayer (or few-layer) structure is maintained before modification. Therefore, Raman spectroscopy was further utilized to measure the number of layers of P123-rGO. As shown in Figure S1, the G band of graphene appeared at 1591 cm^{-1} in the Raman spectrum of P123-rGO, which is consistent with graphene of less than five layers.[34] In addition, the 2D peak located at 2671 cm^{-1} is also a typical feature of 3−5 layered graphene.[35] Therefore, as a kind of porogen for the synthesis of MCFs, the modifier P123 can not only efficiently prevent the aggregation of rGO to maintain its number of layers but also offer a foundation for the in situ growth of MCF outer layers.

The surface morphology of MCFs@rGO was investigated and shown in Figure 1C. It can be observed that the sheetlike contour of this composite is similar to that of the precursor P123-rGO. However, there is a clear difference in terms of the surface morphology. Unlike that of P123-rGO, the surface of MCFs@rGO is evenly covered with a thin layer of mesoporous silicate with a pore size of around 25−30 nm. By comparison, this modified mesoporous silicate exhibited the same disordered pore structure as that of MCFs (Figure 1D), indicating the successful modification of large-diameter foamed silicon MCFs on the template sheet of P123-rGO. Moreover, the difference in contrast between the TEM images of MCFs and those of MCFs@rGO should be noted. It is difficult to form a mesoporous silicate with a specific 2D structure without efficient support.[27,36] Therefore, the contrast of pure MCFs in Figure 1D is observed to be significantly nonuniform, demonstrating that the thickness of conventional MCFs is uncontrollable. However, owing to the immobilized template agent of P123 on rGO, MCFs could be grown in situ on the nanosheet to form a thin outer layer of even thickness, resulting in the uniform contrast exhibited in Figure 1C. By comparison, it is the rGO skeleton that results in the formation of MCFs with specific 2D morphology, which facilitates the electron transfer of immobilized redox enzymes.[37] It should also be noted that the thin MCF@rGO flake can efficiently facilitate the mass-transfer process of enzymatic electrocatalysis. Moreover, the repeatability of the as-prepared modified electrode can also be improved because of the

DOI: 10.1021/acsami.9b08569
ACS Appl. Mater. Interfaces 2019, 11, 29522−29535

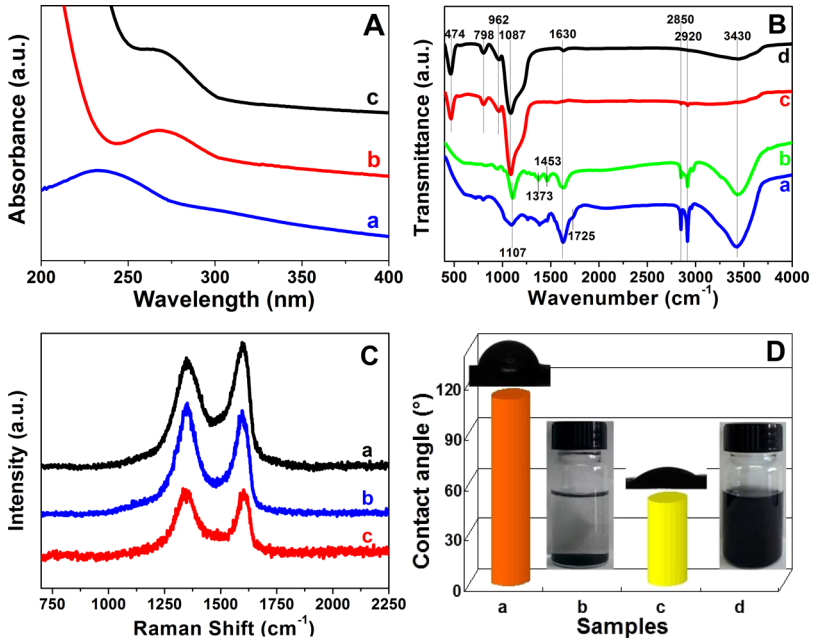

Figure 2. (A) UV−vis absorption spectra of GO (a), P123-rGO (b), MCFs@rGO (c). (B) FTIR spectra of GO (a), P123-rGO (b), MCFs@rGO (c), MCFs (d). (C) Raman spectra of GO (a), rGO (b), MCFs@rGO (c). (D) Contact angles of rGO (a) and MCFs@rGO (c). Photographs of aqueous dispersions of rGO (b) and MCFs@rGO (d).

structural homogeneity of MCFs@rGO. The existence of rGO as an internal support in this flakelike composite was verified by TEM images, as shown in Figure 1E,F. As shown, a small amount of sheetlike rGO is clearly exposed out of the composite, indicating the existence of the rGO nanosheet as a 2D support inside MCFs. The presence of internal rGO can also be demonstrated by the EDS measurement. As shown in the EDS of MCFs (Figure 1G), only characteristic peaks of Si and O are evident at 1.74 and 0.52 keV, respectively. By comparison, a new peak of C located at 0.28 keV, arising from the internal rGO, appeared in the EDS of MCFs@rGO (Figure 1H).

The formation of MCFs@rGO was monitored by UV−vis and FTIR spectra. As shown in curve a of Figure 2A, the original GO exhibited a characteristic absorption peak at 230 nm, attributed to the $\pi \rightarrow \pi^*$ transition of the aromatic C═C band of the nanosheet. After GO was modified with P123, during the reduction process, this characteristic peak red-shifted to 270 nm (curve b of Figure 2A), indicating that the electron conjugation within GO was efficiently recovered because of the reduction treatment. The modifier of rGO was then transferred from the polymer to inorganic MCFs. Curve c shows that the UV−vis spectrum of MCFs@rGO still exhibited a characteristic peak at 270 nm, which is similar to that of the precursor P123-rGO. This result confirms that the internal support of rGO maintains its original structure during the process of inorganic modification, which is conducive to maintaining the inherent conductivity of rGO for electron transfer. The FTIR spectra of various samples are shown in Figure 2B. It can be seen in curve a that GO exhibits characteristic absorption bands which can be attributed to four oxygen-containing groups. These are the stretching vibration band of C−O−C, located at 1107 cm^{-1}; the bending vibration band of C−OH, located at 1630 cm^{-1}; the stretching vibration band of C═O, located at 1725 cm^{-1}; and the stretching vibration band of O−H, located at 3430 cm^{-1}. After the reduction process with P123, it was found that nearly all of the oxygen-containing bands, except the stretching vibration band of C−O−C, weakened or even disappeared in the spectrum of P123-rGO (curve b). The only remaining oxygen-containing band, C−O−C, located at 1107 cm^{-1}, can be attributed to a polymer of modified P123. Such modification of P123 can also be verified via the appearance of the symmetric and asymmetric stretching vibration bands of C−H in methyl groups located at 1373 and 1453 cm^{-1} in curve b. The modifier on rGO was then converted from polymeric to inorganic mesoporous silicate. Accordingly, the FTIR spectrum of MCFs@rGO (curve c) shows that the characteristic bands of C−H belonging to P123 had disappeared, confirming the successful removal of the template agent P123 in MCFs@rGO. Moreover, four new bands are evident in curve c. The bands located at 1087 and 962 cm^{-1} can be attributed to the Si−O−Si stretching vibration of modified MCFs, whereas the bands located at 474 and 798 cm^{-1} can be attributed to the Si−OH stretching vibration of the modifier. The locations of these bands closely coincide with those observed in the FTIR spectrum of MCFs (curve d), clearly illustrating the formation of the inorganic modifier of mesoporous silicate on rGO.

Figure 2C displays the Raman spectra of GO, rGO, and MCFs@rGO. It is well known that the ratio of the intensities of the D and G bands (I_D/I_G) can be used to determine the degree of material reduction for graphene materials. As can be seen in curve a, the I_D/I_G value of GO is estimated to be 0.92. By comparison, this value for rGO was found to increase to 1.12 (curve b), indicating an increase in the conjugated graphene network reconfiguration after reduction. The value of I_D/I_G for MCFs@rGO (curve c) was calculated to be 1.12, which is the same as that of P123-rGO, illustrating that the conjugated structure of rGO was not affected after inorganic modification. In order to observe the possible change in the rGO crystal form after the growth of the MCF modifier, XRD characterizations of rGO and MCFs@rGO were performed. As shown in Figure S2, the diffraction peak of rGO, located at 2θ = 25.3°, is slightly sharper than that of MCFs@rGO, which is

DOI: 10.1021/acsami.9b08569
ACS Appl. Mater. Interfaces 2019, 11, 29522−29535

located at 2θ = 22.8°. Thus, it can be speculated that the crystal form of MCFs@rGO is slightly affected by the inorganic modification of MCFs. This is also consistent with the results of the Raman spectra. Meanwhile, Figure S2 shows that the C(002) peak of MCFs@rGO blue-shifts to a lower angle in comparison to that of rGO, indicating that the layer spacing between rGO nanosheets has been enlarged by the modified outer layer of MCFs.

Given the influence of the surface property of the material on the bioactivity of immobilized proteins, the hydrophilicity of various rGO-based materials was investigated. As shown in image b of Figure 2D, pure rGO without any modification could not be effectively dispersed in aqueous solution; it settled to the bottom of the bottle as a black precipitate. The value of the contact angle of rGO was estimated to be 106°, reflecting the surface hydrophobicity of unmodified rGO. Owing to this inherent hydrophobicity, it is obvious that rGO is not suitable to directly immobilize water-soluble protein. In contrast, it can be seen in image d that MCFs@rGO can be readily dispersed in aqueous solution to form a black dispersion with good homogeneity, indicating that the modified MCF layers endowed rGO with hydrophilicity. As can be seen in Figure S3, the MCF@rGO dispersion is presented as a uniform black dispersion even after standing for 7 days. It can also be observed in column c of Figure 2D that the contact angle of MCFs@rGO greatly decreased (to 49.3°), indicating successful conversion of the surface of rGO, via inorganic modification. The enhancement of hydrophilicity can greatly improve the affinity between immobilized proteins and the matrix, thus providing the proteins with a favorable microenvironment.

3.2. Characterization of the Protein-MCF@rGO Composite. In order to verify the successful immobilization of Hb, especially inside the mesopores of MCFs@rGO, a nitrogen sorption experiment was performed. As shown, the nitrogen adsorption−desorption isotherm of untreated MCFs@rGO (curve a in Figure 3A) exhibits an obvious type IV curve, which indicates a typical mesoporous material.[38] The pore volume and the pore size of MCFs@rGO were measured to be 1.93 $cm^3\ g^{-1}$ and 30.25 nm, respectively, which are consistent with those of the typical MCFs.[39] After the interaction with Hb in aqueous solution, the nitrogen adsorption−desorption isotherm of the Hb-MCFs@rGO obtained is shown as curve b in Figure 3A. As can be seen, the pore volume of MCFs@rGO after immobilization of Hb was found to be reduced to 0.22 $cm^3\ g^{-1}$, which is about 11.4% of the result before enzymatic treatment. Meanwhile, the pore size of MCFs@rGO also decreased significantly from 30.25 to 12.39 nm, indicating that the internal space of mesopores had been successfully occupied by Hb. It is worth noting that curve b is still exhibited as a type IV curve, demonstrating that Hb-MCF@rGO retains mesoporous characteristics after enzymatic immobilization. Such results demonstrate that enough space remains in the mesopores to enable mass transfer during bioelectrocatalysis processes.

After the nitrogen sorption experiment, the corresponding samples were further characterized by EDS. As shown in Figure 3B, three significant peaks attributed to C, O, and Si, located at 0.28, 0.52, and 1.74 keV, respectively, can be observed in the EDS of MCFs@rGO. After treatment with Hb, it can be observed that the L, Kα, and Kβ peaks of Fe, arising from the heme core of Hb, appear at 0.71, 6.41, and 7.06 keV, respectively (Figure 3C). The variation of EDS results clearly

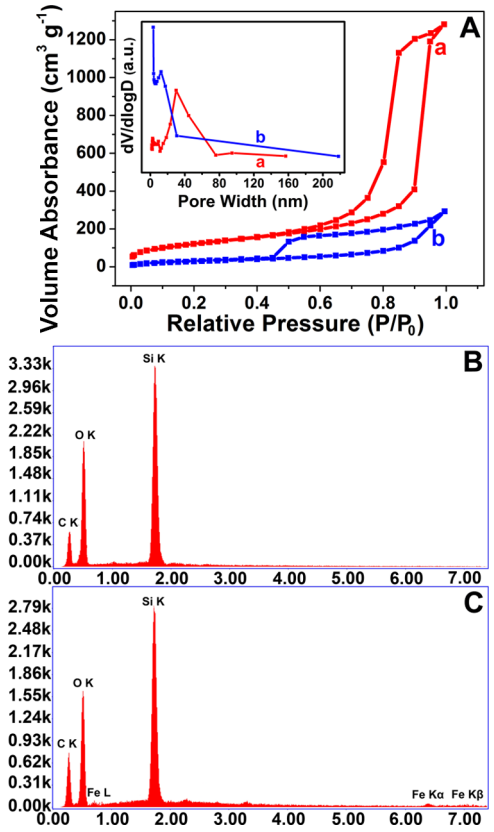

Figure 3. (A) Nitrogen adsorption−desorption isotherms for MCFs@rGO (a) and Hb-MCFs@rGO (b). Pore size distribution of MCFs@rGO (a) and Hb-MCFs@rGO (b) (inset of A). EDS of MCFs@rGO (B) and Hb-MCFs@rGO (C).

indicates the successful immobilization of the redox protein in MCFs@rGO.

The UV−vis spectrum was also analyzed to investigate enzymatic immobilization.[40] Figure 4A shows that there was no absorption band on the MCF@rGO curve (curve c). After MCF@rGO was treated with an aqueous dispersion of Hb, the Soret absorption band of Hb (curve a), located at 405 nm, appeared on its UV−vis spectrum (curve b of Figure 4A), indicating the entrapment of proteins in the hybrid. This typical absorption band of loaded Hb is in agreement with that of free Hb (curve b), demonstrating that the conformational integrity of the protein was not destroyed after immobilization. This can be attributed to the large mesopores of the MCF outer layer, which provides the immobilized Hb with sufficient space and a suitable microenvironment. Because the absorption band of the amide group in the protein can reflect the change in the secondary structure, FTIR spectroscopy was also used to monitor the structural changes in Hb.[41] The results are shown in curve b of Figure 4B. The two characteristic peaks located at 1661 and 1539 cm^{-1} can be attributed to the amide I band (C═O) and amide II band (N−H) of entrapped Hb, respectively. It can be seen that these peaks are substantially the same as the peak positions of the natural Hb depicted in curve a, indicating that the structure of Hb is not destroyed after its immobilization in MCFs@rGO.

It is known that good dispersibility of the electrode material is important for the preparation of a modified electrode with good uniformity and repeatability. The dispersibility of the two protein-MCF@rGO was evaluated by DLS. As shown in

DOI: 10.1021/acsami.9b08569
ACS Appl. Mater. Interfaces 2019, 11, 29522−29535

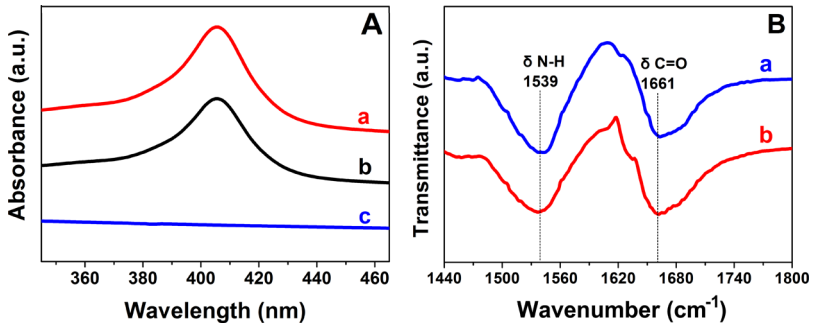

Figure 4. (A) UV−vis absorption spectra of free Hb (a), Hb-MCFs@rGO (b), and MCFs@rGO (c). (B) FTIR spectra of free Hb (a) and Hb-MCFs@rGO (b).

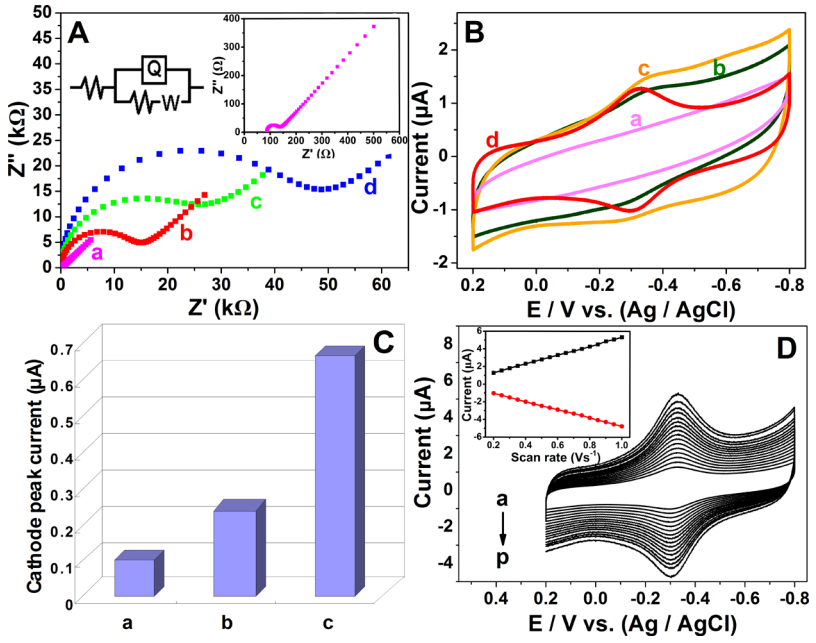

Figure 5. (A) EISs of rGO/GCE (a), MCFs@rGO/GCE (b), MCFs/GCE (c), and Hb-MCFs@rGO/GCE (d) in 10.0 mmol L^{-1} $Fe(CN)_6^{4-/3-}$ (1:1) solution containing 0.10 mol L^{-1} KCl, with a frequency range of 0.1 to 10^5 Hz, an open-circuit potential of 0.2 V, and an amplitude of 5 mV. Insets are equivalent circuit (left) and enlarged EIS of rGO/GCE (right). (B) Cyclic voltammograms of MCFs@rGO/GCE (a), Hb-MCFs/GCE (b), Hb-P123-rGO/GCE (c), and Hb-MCFs@rGO/GCE (d). (C) Cathodic peak currents of Hb-MCFs/GCE (a), Hb-P123-rGO/GCE (b), and Hb-MCFs@rGO/GCE (c). (D) Cyclic voltammograms of Hb-MCFs@rGO/GCE in 0.1 mol L^{-1} pH 7.0 PBS solution with a scan rate range of 0.2−1.0 V s^{-1}. Plot of the cathodic and anodic peak current vs scan rate (inset).

Figure S4, both aqueous suspensions (Hb-MCFs@rGO and GOD-MCFs@rGO) display narrow size distributions, demonstrating good dispersibility of both protein-based composites. The average hydrodynamic sizes and polymer dispersity index (PDI) of the two suspensions are summarized in Table S1. The average hydrodynamic sizes of Hb-MCFs@rGO and GOD-MCFs@rGO are 531.93 and 519.38 nm, respectively.[43] Moreover, it is noticeable that both the PDI values are below 0.5, indicating good dispersibility for both the electrode materials.[42]

One of the purposes of integrating MCFs on rGO was to compensate for the weak conductivity of mesoporous silicates for use in biosensor applications. In order to verify the effect of this integration, EISs of various modified electrodes were investigated. As shown in Figure 5A, the electron-transfer resistances (R_t) of rGO/GCE, MCFs/GCE, and MCFs@rGO/GCE were 45.1, 2.3×10^4, and 1.3×10^4 Ω, respectively. Further, MCFs/GCE displayed the largest R_t because of the weak conductivity of silicate-based MCFs. However, after MCFs were combined with conductive rGO, the R_t of the as-prepared MCFs@rGO/GCE was greatly reduced. This result indicates that the internal rGO backbone provides an efficient inner pathway for electron transfer, which can effectively promote the redox reaction on the modified electrode. In addition, the EIS also verifies the efficient entrapment of Hb into MCFs@rGO. As compared to that of MCFs@rGO/GCE, the R_t of Hb-MCFs@rGO/GCE was found to increase from 2.3×10^4 to 4.2×10^4 Ω, indicating the successful immobilization of Hb into MCFs@rGO.

3.3. Direct Electrochemical Properties and Electrocatalytic Properties of MCFs@rGO/GCE Modified with Protein Containing the Heme Redox Center. As shown in Figure 5B, typical cyclic voltammograms of MCFs@rGO/GCE, Hb-MCFs/GCE, Hb-P123-rGO/GCE, and Hb-MCFs@rGO/GCE were examined over the potential range of +0.2 to −0.8 V in a PBS solution of pH 7.0. No redox peak was observed for MCFs@rGO/GCE (curve a), demonstrating that MCF@rGO was not electroactive in the scanning potential

DOI: 10.1021/acsami.9b08569
ACS Appl. Mater. Interfaces 2019, 11, 29522−29535

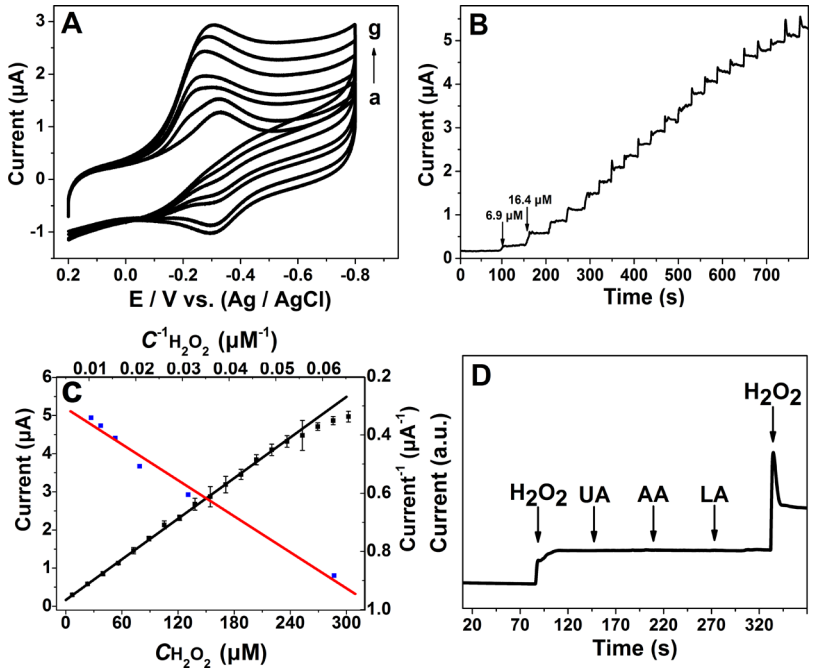

Figure 6. (A) Cyclic voltammograms of Hb-MCFs@rGO/GCE in 0.1 mol L^{-1} PBS solution (pH 7.0) containing 0 (a), 16 (b), 32 (c), 48 (d), 64 (e), 80 (f), and 96 μmol L^{-1} (g) H_2O_2 with a scan rate of 0.2 V s^{-1}. (B) Typical current−time response of Hb-MCFs@rGO/GCE on successive addition of H_2O_2 in stirred 0.1 mol L^{-1} PBS solution (pH 7.0) with an applied potential of −0.48 V. (C) Calibration curve (black) and the Lineweaver−Burk plot (red). (D) Typical current−time response of Hb-MCFs@rGO/GCE on addition of 1 μmol L^{-1} H_2O_2, 20 μmol L^{-1} UA, 20 μmol L^{-1} AA, and 20 μmol L^{-1} LA in stirred 0.1 mol L^{-1} PBS solution (pH 7.0) with an applied potential of −0.48 V.

range. Moreover, it is well known that Hb cannot achieve DET on hydrophobic bare GCE.[13,44] However, after the proteins were immobilized on the various modified electrodes, several quasi-reversible redox peaks were observed for the three modified electrodes of Hb-MCFs/GCE (curve b), Hb-P123-rGO/GCE (curve c), and Hb-MCFs@rGO/GCE (curve d). The formal potential (E_p) of these modified electrodes, calculated from the average value of the cathodic and anodic peak potentials, was −0.33 V.[45] This E_p is characteristic of the reversible electrode process of the heme-Fe(III)/Fe(II) redox couple in immobilized Hb, indicating that efficient DET was achieved between the immobilized Hb and the various modified electrodes.[13] In addition, it is obvious that large differences exist between these Hb electrodes. First, with respect to the potential difference, the differences in the cathodic and anodic peak potentials of Hb-MCFs/GCE, Hb-P123-rGO/GCE, and Hb-MCFs@rGO/GCE were 88, 92, and 31 mV, respectively. The value for Hb-MCFs@rGO/GCE was much smaller than that of Hb-MCFs/GCE and Hb-P123-rGO/GCE, indicating that a faster electron-transfer process was obtained with Hb-MCFs@rGO/GCE, as compared to the other two modified electrodes. Second, the redox peak currents of Hb-MCFs@rGO/GCE were markedly larger than those of Hb-MCFs/GCE and Hb-P123-rGO/GCE. As shown in Figure 5C, the cathodic peak currents of Hb-MCFs/GCE, Hb-P123-rGO/GCE, and Hb-MCFs@rGO/GCE were 0.10, 0.24, and 0.66 μA, respectively. The peak current of Hb-MCFs@rGO/GCE was even larger than that of the sum of the two components-based Hb electrodes: Hb-MCFs/GCE and Hb-P123-rGO/GCE. Considering the significant distinctions in these voltammetric responses, it can be concluded that the integrated composite of MCFs@rGO shows a significant synergistic effect by the two components, facilitating DET between Hb and the underlying electrode. On one hand, MCFs@rGO preserved the excellent biocompatibility of MCFs, maintaining the bioactivity of Hb immobilized on the composite. On the other hand, the internal backbone of rGO endowed the composite with excellent electrical conductivity, facilitating electron transfer.

The direct electrochemical properties of HRP, another redox enzyme with heme as its redox center, were also investigated at the MCF@rGO electrode to estimate the universality of such a hybrid. As shown in Figure S5, a pair of well-defined redox peaks was observed for the modified electrode of HRP-MCFs@rGO. The formal potential (E_p) was calculated as −0.31 V, which is characteristic of the reversible electrode process of the heme-Fe(III)/Fe(II) redox couple in immobilized HRP.[46] Such a result is similar to that observed at the Hb-MCFs@rGO electrode, demonstrating that MCFs@rGO exhibited a universal function of promoting the DET of heme enzymes of different types.

Figure 5D is a typical cyclic voltammogram of Hb-MCFs@rGO/GCE, with a scan rate of 0.2−1.0 V s^{-1} in a PBS solution of pH 7.0. It can be observed that the peak positions of the cathodic and anodic peaks did not change significantly with an increase in sweep rate. Meanwhile, the peak currents of both the anode and cathode increased linearly according to the calibration diagram in Figure 5D. This indicates that the redox reaction of immobilized Hb on MCFs@rGO was a surface-controlled process.[3,7] According to Faraday's law, $Q = nFA\Gamma^*$ (where Q can be determined by calculating the integral of the reduction peak of Hb, n is the number of transferred electrons, F is the Faraday constant, and A is the geometric surface area of the electrode), Γ^*, which is the surface concentration of Hb with electroactivity, was calculated to be 4.37×10^{-11} mol cm^{-2}. This is about 4.1 and 12.3 times higher than that of Hb-P123-rGO/GCE and Hb-MCFs/GCE, respectively.[13] Therefore, it is clear that the electroactivity of Hb was greatly

DOI: 10.1021/acsami.9b08569
ACS Appl. Mater. Interfaces 2019, 11, 29522−29535

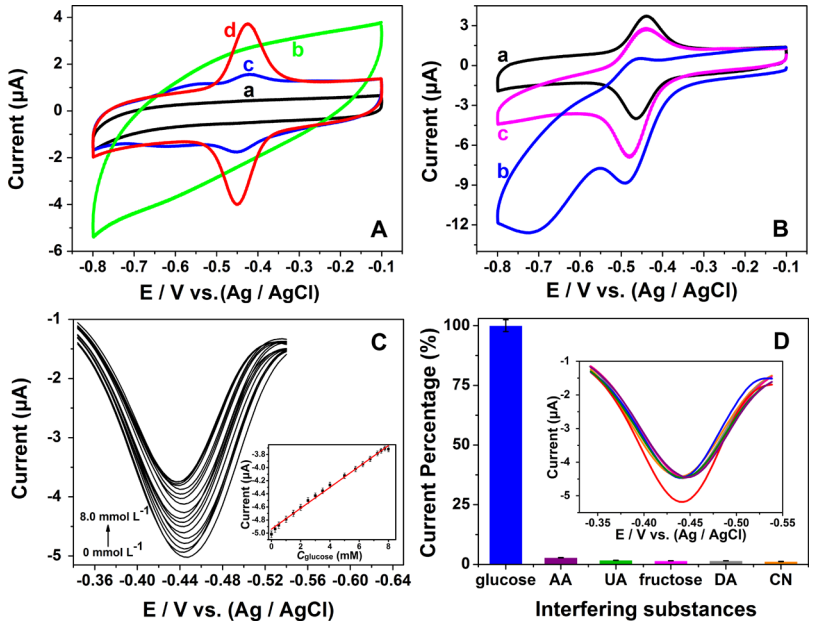

Figure 7. (A) Cyclic voltammograms of MCFs@rGO/GCE (a), GOD-P123-rGO/GCE (b), GOD-MCFs/GCE (c), and GOD-MCFs@rGO/GCE (d) in the potential range of −0.1 to −0.8 V. (B) Cyclic voltammograms of GOD-MCFs@rGO/GCE in nitrogen-saturated (a) and air-saturated (b) glucose-free PBS solution (pH 7.4) and air-saturated PBS solution (pH 7.4) with 3.0 mmol L^{-1} glucose present (c). (C) DPV curves of GOD-MCFs@rGO/GCE in air-saturated PBS solutions (pH 7.4) containing 0, 0.25, 0.50, 0.75, 1.25, 1.75, 2.25, 2.75, 3.25, 3.75, 4.25, 4.75, 5.25, 5.75, 6.25, 7.25, 7.50, 7.75, 8.00 mmol L^{-1} glucose in the potential range of −0.34 to −0.54 V. Plot of the peak current vs glucose concentrations (inset). (D) DPV peak current responses of GOD-MCFs@rGO/GCE to 2.0 mmol L^{-1} pure glucose solution and 2.0 mmol L^{-1} glucose solution containing 0.2 mmol L^{-1} AA, UA, fructose, DA, and CN, respectively. DPV curves of GOD-MCFs@rGO/GCE in PBS solution (red line), 2.0 mmol L^{-1} pure glucose solution (blue line), and 2.0 mmol L^{-1} glucose solutions containing 0.2 mmol L^{-1} AA (purple line), UA (green line), fructose (pink line), DA (gray line), and CN (orange line), respectively (inset).

improved after immobilization of Hb into MCFs@rGO, indicating that this composite provides both a favorable microenvironment and an efficient electron-transfer tunnel for the immobilized proteins. Moreover, this value is also about 2.3 times higher than the theoretical monolayer surface concentration of Hb (1.89×10^{-11} mol cm^{-2}), demonstrating that the multiple layers of Hb in MCFs@rGO participated in the process of DET.[13,47] The apparent electron-transfer rate constant (k_s) of the redox reaction of Hb was calculated according to Laviron's equation ($n\Delta E_p \leq 200$ mV) as follows

$$\log k_s = \alpha \log(1-\alpha) + (1-\alpha)\log \alpha - \log \frac{RT}{nFv} - \frac{\alpha(1-\alpha)nF\Delta E_p}{2.3RT} \quad (1)$$

where α is calculated to be 0.66 by the slope of the linear curve.[47] The k_s was calculated to be 11.57 s^{-1}, which is higher than for several reported graphene-based Hb electrodes, such as Nafion/Hb/H-TiO_2-rGOMS/GCE (3.27 s^{-1}), CTS/Hb/GR-CuS/CILE (1.58 s^{-1}), CTS-NG-Hb/CILE (2.36 s^{-1}), and Nafion/GR-TiO_2/CILE (0.65 s^{-1}).[13,48−50] This result indicates that a fast electron-transfer process occurs at Hb-MCFs@rGO/GCE. The fast electron transfer of Hb can be ascribed to the high affinity between entrapped proteins and the matrix of MCFs@rGO.

Taking H_2O_2 as the model, the bioelectrocatalytic performance of Hb-MCFs@rGO/GCE was investigated. Specifically, H_2O_2 was continuously added to 0.1 mol L^{-1} PBS solution of pH 7.0 in order to examine the reduction of H_2O_2 with a CV of Hb-MCFs@rGO/GCE. As can be seen in Figure 6A, when H_2O_2 was continuously added, a significant decrease in the oxidation peak current and an increase in the reduction peak current occurred on the CV curve of Hb-MCFs@rGO/GCE. The reason for this phenomenon is that when Hb−Fe(III) is reduced to Hb−Fe(II) by DET, the resulting Hb−Fe(II) can be oxidized by H_2O_2 and converted back into Hb−Fe(III).[50] This indicates that Hb-MCFs@rGO/GCE retained its bioelectrocatalytic activity toward the reduction of H_2O_2. The catalytic performance of Hb-MCFs@rGO/GCE was further investigated by chronoamperometry at a potential of −0.48 V.[51] As shown in Figure 6B, Hb-MCFs@rGO/GCE displayed a fast response time of 6 s to achieve 95% of steady-state current, owing to the easy diffusion of H_2O_2 in the MCF layers with large mesopores. In addition, the amperometric currents obtained at Hb-MCFs@rGO/GCE are proportional to the H_2O_2 concentration. It can be seen in Figure 6C that the current response of Hb-MCFs@rGO/GCE increased linearly with H_2O_2 concentration ranging from 6.9 to 270 μmol L^{-1}. The linear regression equation is $y = 0.0177x + 0.176$ ($R = 0.999$, $n = 14$), where y is the peak current (μA) and x is the H_2O_2 concentration (μmol L^{-1}). The sensitivity was calculated to be 0.25 μA μmol^{-1} L cm^{-2}. Moreover, the detection limit was estimated to be 63.6 nmol L^{-1} based on S/N = 3, which is much lower than that of reported mesoporous material-based Hb electrodes.[27,52−55]

This low detection limit can be attributed to the electron-transfer capacity arising from the inner rGO backbone. The apparent Michaelis−Menten constant (K_M^{app}) calculated from Laviron's equation was 49.05 μmol L^{-1}, which is also much lower than that of reported mesoporous silicate- or rGO-based Hb electrodes, such as Hb/multiwalled carbon nanotubes (MWCNTs)-MCM41/GCE, Hb/porous Pd@Fe_3O_4-MWCNT, Hb/H-TiO_2-rGOMS/GCE, and Hb/P123-NGP/

DOI: 10.1021/acsami.9b08569
ACS Appl. Mater. Interfaces 2019, 11, 29522−29535

GCE.[14−16,29] Such a low K_M^{app} indicates a high affinity between the immobilized Hb and MCFs@rGO, which can be ascribed to the favorable microenvironment provided by the large mesopores. Detailed comparisons between MCFs@rGO/GCE and other Hb-based electrodes with respect to electrochemical performance are provided in Table S2. Chronoamperometry was also utilized to examine the interference of Hb-MCFs@rGO/GCE by uric acid (UA), ascorbic acid (AA), and lactic acid (LA). As shown in Figure 6D, Hb-MCFs@rGO/GCE only exhibited a sensitive and fast response toward the added target analyte of H_2O_2. No current response was observed with the addition of various interfering substances, indicating excellent selectivity of Hb-MCFs@rGO/GCE.

3.4. Direct Electrochemical Properties and Electrocatalytic Properties of MCFs@rGO/GCE Modified with Enzymes Containing the FAD Redox Center. The possibility of MCFs@rGO enhancing the DET of enzymes with FAD as their redox center was further investigated. As one of the typical FAD-based redox enzymes that can oxidize glucose to gluconic acid, GOD was first utilized to construct a modified electrode with MCFs@rGO.[57] The achievement of GOD-MCFs@rGO/GCE with amplified DET signal can not only simplify the bioanalysis system but also improve the analytical performance for the detection of blood glucose.

As shown in Figure 7A, typical CVs of MCFs@rGO/GCE, GOD-MCFs/GCE, GOD-P123-rGO/GCE, and GOD-MCFs@rGO/GCE were examined over the potential range of −0.1 to −0.8 V in a PBS solution of pH 7.4. Similar to those observed at Hb-P123-rGO/GCE, no redox peak was observed at both MCFs@rGO/GCE (curve a) and GOD-P123-rGO/GCE (curve b). However, a pair of quasi-reversible redox peaks was observed for GOD-MCFs/GCE (curve c) and GOD-MCFs@rGO/GCE (curve d) respectively. The formal potentials (E_p) of the two modified electrodes were −0.44 V, which is characteristic of the reversible electrode process of the $FAD/FADH_2$ redox couple in immobilized GOD.[57] This result indicates that the immobilized GOD can easily achieve efficient DET on both MCFs and MCFs@rGO-modified electrodes. It is worth noting that the redox peak currents of GOD-MCFs@rGO/GCE were markedly larger than that of GOD-MCFs/GCE, demonstrating that MCFs@rGO can facilitate DET between GOD and the underlying electrode more effectively.

The estimation of MCFs@rGO for the DET promotion of other redox enzymes with the FAD center was further investigated using ChOx as an example. Similar to that observed at GOD-MCFs@rGO/GCE, a pair of quasi-reversible redox peaks can also be easily observed at ChOx-MCFs@rGO/GCE in Figure S6. The E_p was estimated to be −0.45 V, which is characteristic of the reversible electrode process of the $FAD/FADH_2$ redox couple in immobilized ChOx.[59,60] Such a result indicates that efficient DET can be achieved between the immobilized ChOx and electrode with the assistance of MCFs@rGO.

Typical CVs of the GOD-MCFs@rGO/GCE, with a scan rate of 0.1−1.0 V s^{-1} in PBS solution (pH 7.4), are shown in Figure S7. The peak currents of both the anode and cathode peaks increased linearly according to the calibration diagram in the inset of Figure S7, indicating that the redox reaction of immobilized GOD on MCFs@rGO was a surface-controlled process.[3,7] According to Faraday's law of $Q = nFA\Gamma^*$, the surface concentration of GOD was calculated to be 1.36×10^{-10} mol cm^{-2}, which is close to the theoretical monolayer surface concentration of GOD (1.70×10^{-10} mol cm^{-2}). This result demonstrates that the single layer of GOD in MCFs@rGO participated in the process of DET.[53]

The electrocatalytic properties of GOD-MCFs@rGO/GCE with respect to glucose oxidation were investigated by CV and DPV. As can be seen in Figure 7B, the CV curve of GOD-MCFs@rGO/GCE exhibits a good pair of redox peaks in a nitrogen-saturated PBS solution of pH 7.4 (curve a). By comparison, curve b shows an obvious increase of the reduction peak current and a decrease of oxidation peak current under the condition of air saturation. This is due to the reduction of oxygen in the solution. However, when 3.0 mmol L^{-1} glucose was added to the air-saturated PBS solution (curve c), the reduction peak current showed a significant decrease, as compared to that of curve b. It can be ascribed to the mechanism of action of GOD as follows:[57]

$$\text{Glucose} + \text{GOD(FAD)} \rightarrow \text{Gluconic acid} + \text{GOD}(FADH_2) \quad (2)$$

$$\text{GOD}(FADH_2) + O_2 \rightarrow \text{GOD(FAD)} + H_2O_2 \quad (3)$$

The bioelectrocatalytic performance of GOD-MCFs@rGO/GCE was further investigated by DPV. Specifically, DPV curves of 0.1 mol L^{-1} PBS solutions (pH 7.4) with the continuous addition of glucose were measured in the potential range of −0.34 to −0.54 V. As shown in Figure 7C, a significant decrease in the reduction peak current occurred on the DPV curve of GOD-MCFs@rGO/GCE, which can be ascribed to the reduction of GOD-FAD to $GOD\text{-}FADH_2$ by DET.[58] As can be seen in the inset of Figure 7C, the current response of GOD-MCFs@rGO/GCE decreased linearly with glucose concentrations ranging from 0.25 to 8.0 mmol L^{-1}. The linear regression equation is $y = 0.160x - 4.94$ ($R = 0.998$, $n = 18$), where y is the peak current (μA) and x is the glucose concentration (mmol L^{-1}). This linear range is wider than those of reported mesoporous materials or carbon material-based GOD electrodes.[56,61−66] The wide linear range can be attributed to the biocompatibility and inner conductivity of MCFs@rGO. It is known that the range of normal blood glucose concentration is 3.9−6.2 (empty stomach) mmol L^{-1}.[67] Blood glucose concentrations above and below this range are characteristic of diabetes and hypoglycemia, respectively.[68] From this point of view, the linear range of GOD-MCFs@rGO/GCE covers the range of practical blood glucose concentrations, demonstrating its potential application for the detection of blood glucose of real samples. In addition, the sensitivity and detection limit of GOD-MCFs@rGO/GCE were calculated to be 2.257 μA $mmol^{-1}$ L cm^{-2} and 98.4 μmol L^{-1} (S/N = 3), respectively.

DPV was also utilized to investigate the selectivity of GOD-MCFs@rGO/GCE. The DPV response to some possible coexisting substances, such as UA, AA, dopamine (DA), fructose, and creatinine (CN), was measured. As shown in Figure 7D, the current value was significantly reduced by 0.4 μA after the addition of 2.0 mmol L^{-1} glucose. In comparison, the current responses in the presence of various interfering substances were all below 3% compared with that of pure glucose, indicating that GOD-MCF@rGO/GCE exhibits excellent selectivity.

3.5. Detection of Blood Glucose in Human Serum Based on GOD-MCFs@rGO/GCE. To further study the potential applications of GOD-MCFs@rGO/GCE, the detec-

DOI: 10.1021/acsami.9b08569
ACS Appl. Mater. Interfaces 2019, 11, 29522−29535

tion of blood glucose in real samples of human serum was performed. The concentrations of blood glucose in three human serum samples were measured by GOD-MCFs@rGO/GCE as well as by a commercially available blood glucose meter. The corresponding results are listed in Table S3. As can be seen, the concentrations of blood glucose measured by GOD-MCFs@rGO/GCE are basically consistent with those detected by the blood glucose meter. For each sample, the relative standard deviation was below 3.5%, indicating that GOD-MCFs@rGO/GCE is reliable and effective for use in the practical detection of blood glucose.

Although both the established GOD-MCFs@rGO/GCE and commercially available glucose meters can achieve accurate detection of blood glucose in biological samples, there are still distinct differences between them. Most importantly, the structure and mechanisms of the two biosensors are quite different. Commercially available glucose meters belong to the second-generation class of biosensors, which use an electrochemical mediator.[69] They rely on the assistance of the mediator to transfer electrons from the enzyme to the surface of the electrode. However, being a typical third-generation biosensor, GOD-MCFs@rGO/GCE is mediator-free. The analytical signal at this type of electrode is obtained via the DET between the enzyme and the electrode. Because of this, improved analytical performance can be achieved by GOD-MCFs@rGO/GCE in comparison to glucose meters, as the electron transmission, being independent of a mediator, is more efficient. Moreover, some defects related to the mediator can also be avoided by the use of third-generation biosensors, such as the loss of soluble mediator in solution and the absence of a diffusion barrier between the mediator and enzyme−electrode interface.[69] Table S4 exhibits a comparison between GOD-MCFs@rGO/GCE and various commercially available blood glucose meters in terms of quantification limit. It can be seen that the quantification limit of the modified electrode in our work is only 0.25 mmol L^{-1}, which is much lower than those of second-generation blood glucose meters.

3.6. Stability and Reproducibility of Hb-MCFs@rGO/GCE and GOD-MCFs@rGO/GCE. It is known that the thermal stability of an immobilized enzyme can be greatly enhanced by protecting it with biocompatible mesopores, thus leading to the possible utilization of the corresponding biosensor under extreme conditions. Accordingly, the effect of temperature on the electrocatalysis of GOD-MCFs@rGO/GCE was investigated by CV in the presence of 3.0 mM glucose. GOD-MCFs@rGO/GCE was heated for 15 min in 0.1 mol L^{-1} PBS solution (pH 7.4) at a temperature range of 25−75 °C. The residual activity of immobilized GOD is expressed as the ratio of the current response of the modified electrode (I_{cat}) before and after thermal treatment. As shown in Figure S8, the residual activity of GOD decreased slightly after thermal treatment at 35, 45, 55, and 65 °C. After heating at 75 °C, the immobilized GOD still retained the residual activity of 54%. By comparison, the corresponding residual activity of native GOD is reported to be less than 10% after heating for 5 min at 75 °C.[70] Such results demonstrate that the thermal stability of GOD significantly improved its entrapment into the outer layer of MCFs@rGO, which may be due to the confined space and biocompatible microenvironment provided by the mesopores.

The stability and reproducibility of Hb-MCFs@rGO/GCE and GOD-MCFs@rGO/GCE were also investigated, respectively. The CV peak currents of Hb-MCFs@rGO/GCE and GOD-MCFs@rGO/GCE were measured after continuous scanning for 100 cycles in the range of +0.2 to −0.8 V and −0.1 to −0.8 V, with a scan rate of 0.2 V s^{-1}. It was found that the current values of both electrodes were well maintained, indicating that Hb-MCFs@rGO/GCE and GOD-MCFs@rGO/GCE are stable in PBS solutions. Moreover, the electrocatalytic responses of the two modified electrodes were investigated after storage for 15 days. As shown in Figure S9, the CV curve of Hb-MCFs@rGO/GCE displayed a slightly weaker current response, as compared with the original signal of the curve measured before storage. The signal decline was estimated to be less than 5% for 64 μmol L^{-1} H_2O_2. A similar result was observed on DPV curves of GOD-MCFs@rGO/GCE, in that the current response for 2.0 mmol L^{-1} glucose was reduced by less than 5% after storage. These results suggest that both the modified electrodes exhibit excellent long-term stabilities. The good long-term stability can be attributed to the favorable microenvironment of the entrapped redox protein provided by the MCF outer layer. To investigate the reproducibility of the results for the modified electrodes, CV of Hb-MCFs@rGO/GCE and DPV of GOD-MCFs@rGO/GCE were independently performed for five modified electrodes made from the same GCE. As for Hb-MCFs@rGO/GCE and GOD-MCFs@rGO/GCE, acceptable reproducibilities with relative standard deviations of 4.2 and 4.5% were found for the currents at 64 μmol L^{-1} H_2O_2 and 2.0 mmol L^{-1} glucose, respectively.

4. CONCLUSIONS

In summary, a novel MCF@rGO composite with a unique sandwich structure was fabricated based on the in situ growth of mesoporous silicate modifiers on both sides of an rGO nanosheet. The organized integration of MCFs and rGO efficiently compensated for the inherent disadvantages of each component. Because of the biocompatibility of the MCF outer layer and the conductivity of the inner skeleton of rGO, various types of redox enzymes, whether containing heme or FAD redox centers, easily achieved enhanced DET at the MCFs@rGO-modified electrode. In comparison to those of the components-based Hb or GOD electrodes, both Hb-MCFs@rGO/GCE and GOD-MCFs@rGO/GCE displayed better preservation of the bioactivity of entrapped redox proteins and achieved improved electrocatalytic performance for the detection of both H_2O_2 and glucose, including good sensitivities and wide linear ranges. Blood glucose in human serum samples was successfully determined with GOD-MCFs@rGO/GCE, making it potentially suitable for the application of blood glucose monitoring, with a low quantification limit. Moreover, GOD-MCFs@rGO/GCE also displayed excellent thermal stability, leading to the conclusion that analytical detection can be achieved even under extreme conditions. This integrated composite with a unique sandwich structure is not only suitable for wide applications in biosensors and biocatalysis but also has valuable potential applications in biomedical devices and bioelectronics.

■ ASSOCIATED CONTENT

Supporting Information

The Supporting Information is available free of charge on the ACS Publications website at DOI: 10.1021/acsami.9b08569.

DOI: 10.1021/acsami.9b08569
ACS Appl. Mater. Interfaces 2019, 11, 29522−29535

Raman spectrum of P123-rGO; XRD patterns of rGO and MCFs@rGO; photograph of the aqueous dispersion of MCFs@rGO after standing for 7 days; hydrodynamic size distributions of suspensions of Hb-MCFs@rGO and GOD-MCFs@rGO; cyclic voltammograms of HRP-MCFs@rGO/GCE; cyclic voltammogram of ChOx-MCFs@rGO/GCE; cyclic voltammograms of GOD-MCFs@rGO/GCE with different scan rates and plot of the cathodic and anodic peak current vs scan rate; effect of the temperature on the activity of GOD-MCFs@rGO/GCE with 3.0 mmol L^{-1} glucose; cyclic voltammograms of Hb-MCFs@rGO/GCE with 64 μmol L^{-1} H_2O_2 on the first day and after being stored for 15 days; average hydrodynamic sizes and PDI values of suspensions of Hb-MCFs@rGO and GOD-MCFs@rGO; comparison of the electrochemical performance between Hb/MCFs@rGO/GCE and the previously reported Hb-based electrodes for the determination of H_2O_2; comparison of results of blood glucose in human serum detected by GOD-MCFs@rGO/GCE and blood glucose meter; and comparison of the quantitation limits between blood glucose meters based on second-generation biosensors and GOD-MCFs@rGO/GCE (PDF)

AUTHOR INFORMATION

Corresponding Authors

*E-mail: zhangq@lnu.edu.cn (Q.Z.).
*E-mail: lixinxia@lnu.edu.cn (L.X.).

ORCID

Qian Zhang: 0000-0002-9741-6349

Author Contributions

The manuscript was written through contributions of all authors. All authors have given approval to the final version of the manuscript.

Notes

The authors declare no competing financial interest.

ACKNOWLEDGMENTS

H.W., F.T., Q.Z., H.Z., T.P., S.L., and L.X. received funding from the National Natural Science Foundation of China (21671089), the Shenyang Natural Science Foundation of China (F16-103-4-00), and the Scientific Research Fund of Liaoning Provincial Education Department (LT2017010, 20170540409). L.Z. and Q.Z. received funding from the Scientific Research Fund of Liaoning Provincial Education Department (LFW201706).

REFERENCES

(1) Li, J.; Cheng, G.; Dong, S. Direct Electron Transfer to Cytochrome C Oxidase in Self-Assembly Monolayers on Gold Electrode. *J. Electroanal. Chem.* **1996**, *416*, 97−104.

(2) Lu, X.; Wen, Z.; Li, J. Hydroxyl-Containing Antimony Oxide Bromide Nanorods Combined with Chitosan for Biosensors. *Biomaterials* **2006**, *27*, 5740−5747.

(3) Zhang, Q.; Qiao, Y.; Hao, F.; Zhang, L.; Wu, S.; Li, Y.; Li, J.; Song, X.-M. Fabrication of a Biocompatible and Conductive Platform based on a Singlestranded DNA/Graphene Nanocomposite for Direct Electrochemistry and Electrocatalysis. *Chem.—Eur. J.* **2010**, *16*, 8133−8139.

(4) Lad, U.; Khokhar, S.; Kale, G. M. Electrochemical Creatinine Biosensors. *Anal. Chem.* **2008**, *80*, 7910−7917.

(5) Jin, Y.; Li, H. Y.; Ping, L. Label-Free Electrochemical Selection of G-Quadruplex-Binding Ligands based on Structure Switching. *Biosens. Bioelectron.* **2010**, *25*, 2669−2674.

(6) Liu, Y.; Shi, L.; Wang, M.; Li, Z.; Liu, H.; Li, J. A Novel Room Temperature Ionic Liquid Sol-gel Matrix for Amperometric Biosensor Application. *Green Chem.* **2005**, *7*, 655−658.

(7) Zhang, L.; Zhang, Q.; Lu, X.; Li, J. Direct Electrochemistry and Electrocatalysis based on Film of Horseradish Peroxidase Intercalated into Layered Titanate Nano-Sheets. *Biosens. Bioelectron.* **2007**, *23*, 102−106.

(8) Krishnan, S. K.; Prokhorov, E.; Bahena, D.; Esparza, R.; Meyyappan, M. Chitosan-Covered Pd@Pt Core-Shell Nanocubes for Direct Electron Transfer in Electrochemical Enzymatic Glucose Biosensor. *ACS Omega* **2017**, *2*, 1896−1904.

(9) Liu, H.; Duan, C.; Su, X.; Dong, X.; Huang, Z.; Shen, W.; Zhu, Z. A Hemoglobin Encapsulated Titania Nanosheet Modified Reduced Graphene Oxide Nanocomposite As a Mediator-Free Biosensor. *Sens. Actuators, B* **2014**, *203*, 303−310.

(10) Si, P.; Ding, S.; Yuan, J.; Lou, X. W.; Kim, D.-H. Hierarchically Structured One-Dimensional TiO_2 for Protein Immobilization, Direct Electrochemistry, and Mediator-Free Glucose Sensing. *ACS Nano* **2011**, *5*, 7617−7626.

(11) Xu, S.; Minteer, S. D. Investigating the Impact of Multi-Heme Pyrroloquinoline Quinone-Aldehyde Dehydrogenase Orientation on Direct Bioelectrocatalysis via Site Specific Enzyme Immobilization. *ACS Catal.* **2013**, *3*, 1756−1763.

(12) Liu, H.; Guo, K.; Duan, C.; Dong, X.; Gao, J. Hollow TiO_2 Modified Reduced Graphene Oxide Microspheres Encapsulating Hemoglobin for a Mediator-Free Biosensor. *Biosens. Bioelectron.* **2017**, *87*, 473−479.

(13) Eguílaz, M.; Villalonga, R.; Rivas, G. Electrochemical Biointerfaces Based on Carbon Nanotubes-Mesoporous Silica Hybrid Material: Bioelectrocatalysis of Hemoglobin and Biosensing Applications. *Biosens. Bioelectron.* **2018**, *111*, 144−151.

(14) Xu, X. X.; Zhang, J. X.; Guo, F.; Zheng, W.; Zhou, H. M.; Wang, B. L.; Zheng, Y. F.; Wang, Y. B.; Cheng, Y.; Lou, X.; Jang, B. Z. A Novel Amperometric Hydrogen Peroxide Biosensor Based on Immobilized Hb in Pluronic P123-Nanographene Platelets Composite. *Colloids Surf., B* **2011**, *84*, 427−432.

(15) Chen, D.; Feng, H.; Li, J. Graphene Oxide: Preparation, Functionalization, and Electrochemical Applications. *Chem. Rev.* **2012**, *112*, 6027−6053.

(16) Sun, M.; Li, J. Graphene Oxide Membranes: Functional Structures, Preparation and Environmental Applications. *Nano Today* **2018**, *20*, 121−137.

(17) Huang, X.; Qi, X.; Boey, F.; Zhang, H. Graphene-based Composites. *Chem. Soc. Rev.* **2012**, *41*, 666−686.

(18) Luo, Z.; Yang, D.; Qi, G.; Yuwen, L.; Zhang, Y.; Weng, L.; Wang, L.; Huang, W. Preparation of Highly Dispersed Reduced Graphene Oxide Decorated with Chitosan Oligosaccharide as Electrode Material for Enhancing the Direct Electron Transfer of Escherichia Coli. *ACS Appl. Mater. Interfaces* **2015**, *7*, 8539−8544.

(19) Yang, J.; Heo, M.; Lee, H. J.; Park, S.-M.; Kim, J. Y.; Shin, H. S. Reduced Graphene Oxide (rGO)-Wrapped Fullerene (C_{60}) Wires. *ACS Nano* **2011**, *5*, 8365−8371.

(20) Ueda, A.; Kato, D.; Kurita, R.; Kamata, T.; Inokuchi, H.; Umemura, S.; Hirono, S.; Niwa, O. Efficient Direct Electron Transfer with Enzyme on a Nanostructured Carbon Film Fabricated with a Maskless Top-Down UV/Ozone Process. *J. Am. Chem. Soc.* **2011**, *133*, 4840−4846.

(21) Wooten, M.; Karra, S.; Zhang, M.; Gorski, W. On the Direct Electron Transfer, Sensing, and Enzyme Activity in the Glucose Oxidase/Carbon Nanotubes System. *Anal. Chem.* **2014**, *86*, 752−757.

(22) Zhao, C.; Wang, Q.; Zhang, H.; Passerini, S.; Qian, X. Two-Dimensional Titanium Carbide/rGO Composite for High-Performance Supercapacitors. *ACS Appl. Mater. Interfaces* **2016**, *8*, 15661−15667.

DOI: 10.1021/acsami.9b08569
ACS Appl. Mater. Interfaces 2019, 11, 29522−29535

(23) Ali, H.; Kanodarwala, F. K.; Majeed, I.; Stride, J. A.; Nadeem, M. A. La_2O_3 Promoted Pd/rGO Electro-Catalysts for Formic Acid Oxidation. *ACS Appl. Mater. Interfaces* **2016**, *8*, 32581−32590.
(24) Wang, C.-I.; Periasamy, A. P.; Chang, H.-T. Photoluminescent C-dots@rGO Probe for Sensitive and Selective Detection of Acetylcholine. *Anal. Chem.* **2013**, *85*, 3263−3270.
(25) Cheong, J. L.; Shao, Y.; Tan, S. J. R.; Li, X.; Zhang, Y.; Su, S. L. Highly Active and Selective Zr/MCF Catalyst for Production of 1,3-Butadiene from Ethanol in a Dual Fixed Bed Reactor System. *ACS Sustain. Chem. Eng.* **2016**, *4*, 4887−4894.
(26) Li, J.; Zhou, L.; Han, X.; Hu, J.; Liu, H.; Xu, J. Direct Electrochemistry of Hemoglobin Immobilized on Siliceous Mesostructured Cellular Foam. *Sens. Actuators, B* **2009**, *138*, 545−549.
(27) Zhang, X.; Zhang, F.; Chan, K.-Y. Synthesis and Characterization of Amino-Functionalized Mesostructured Cellular Foams with Large Mesopores Using Microemulsion Templating. *Scr. Mater.* **2004**, *51*, 343−347.
(28) Zhang, Y.; Wang, Q.; Li, J.; Wang, X.; Liu, K.; Feng, H.; Jiang, J.; Li, J.; Qian, D. Facile Fabrication of Sandwich-Structured Co_3O_4/N-rGO/AB Hybrid with Enhanced ORR Electrocatalytic Performances for Metal-Air Batteries. *RSC Adv.* **2015**, *5*, 9057−9063.
(29) Yang, S.; Cao, C.; Huang, P.; Peng, L.; Sun, Y.; Wei, F.; Song, W. Sandwich-Like Porous TiO_2/Reduced Graphene Oxide (rGO) for High-Performance Lithium-Ion Batteries. *J. Mater. Chem. A* **2015**, *3*, 8701−8705.
(30) Liu, Y.; Li, W.; Shen, D.; Wang, C.; Li, X.; Pal, M.; Zhang, R.; Chen, L.; Yao, C.; Wei, Y.; Li, Y.; Zhao, Y.; Zhu, H.; Wang, W.; El-Toni, A. M.; Zhang, F.; Zhao, D. Synthesis of Mesoporous Silica/Reduced Graphene Oxide Sandwich-Like Sheets with Enlarged and "Funneling" Mesochannels. *Chem. Mater.* **2015**, *27*, 5577−5586.
(31) Xu, Q.; Shen, Y.; Tang, J.; Xue, M.-H.; Jiang, L.; Hu, X. Electrochemical Method Assisted Immobilization and Orientation of Myoglobin into Biomimetic Brij 56 Film and its Direct Electrochemistry Study. *ACS Appl. Mater. Interfaces* **2015**, *7*, 11286−11293.
(32) Hummers, W. S.; Offeman, R. E. Preparation of Graphitic Oxide. *J. Am. Chem. Soc.* **1958**, *80*, 1339.
(33) Li, J.; Li, L.; Zhang, B.; Yu, M.; Ma, H.; Zhang, J.; Zhang, C.; Li, J. Synthesis of Few-Layer Reduced Graphene Oxide for Lithium-Ion Battery Electrode Materials. *Ind. Eng. Chem. Res.* **2014**, *53*, 13348−13355.
(34) Zhang, X.; Li, K.; Li, H.; Lu, J. Dipotassium Hydrogen Phosphate as Reducing Agent for the Efficient Reduction of Graphene Oxide Nanosheets. *J. Colloid Interface Sci.* **2013**, *409*, 1−7.
(35) Wojtoniszak, M.; Chen, X.; Kalenczuk, R. J.; Wajda, A.; Łapczuk, J.; Kurzewski, M.; Drozdzik, M.; Chu, P. K.; Borowiak-Palen, E. Synthesis, Dispersion, and Cytocompatibility of Graphene Oxide and Reduced Graphene Oxide. *Colloids Surf., B* **2012**, *89*, 79−85.
(36) Jiang, F.; Liu, Y.; Wang, X.; Yin, Z. pH-Sensitive Release of Insulin-Loaded Mesoporous Silica Particles and its Coordination Mechanism. *Eur. J. Pharm. Sci.* **2018**, *119*, 1−12.
(37) Liang, B.; Guo, X.; Fang, L.; Hu, Y.; Yang, G.; Zhu, Q.; Wei, J.; Ye, X. Study of Direct Electron Transfer and Enzyme Activity of Glucose Oxidase on Graphene Surface. *Electrochem. Commun.* **2015**, *50*, 1−5.
(38) Cychosz, K. A.; Guillet-Nicolas, R.; García-Martínez, J.; Thommes, M. Recent Advances in the Textural Characterization of Hierarchically Structured Nanoporous Materials. *Chem. Soc. Rev.* **2017**, *46*, 389−414.
(39) Feng, X.; Hu, G.; Hu, X.; Xie, G.; Xie, Y.; Lu, J.; Luo, M. Tetraethylenepentamine-Modified Siliceous Mesocellular Foam (MCF) for CO_2 Capture. *Ind. Eng. Chem. Res.* **2013**, *52*, 4221−4228.
(40) Zhang, Q.; Zhang, L.; Liu, B.; Lu, X.; Li, J. Assembly of Quantum Dots-Mesoporous Silicate Hybrid Material for Protein Immobilization and Direct Electrochemistry. *Biosens. Bioelectron.* **2007**, *23*, 695−700.
(41) Zhang, Q.; Zhang, L.; Li, J. DNA-Hemoglobin-Multiwalls Carbon Nanotube Hybrid Material with Sandwich Structure: Preparation, Characterization, and Application in Bioelectrochemistry. *J. Phys. Chem. C* **2007**, *111*, 8655−8660.
(42) Wittmar, A.; Gajda, M.; Gautam, D.; Dörfler, U.; Winterer, M.; Ulbricht, M. Influence of The Cation Alkyl Chain Length of Imidazolium-Based Room Temperature Ionic Liquids on The Dispersibility of TiO_2 nanopowders. *J. Nanopart. Res.* **2013**, *15*, 1463.
(43) Ma, J.; Liu, J.; Zhu, W.; Qin, W. Solubility Study on The Surfactants Functionalized Reduced Graphene Oxide. *Colloids and Surfaces, A: Physicochemical and Engineering Aspects* **2018**, *538*, 79−85.
(44) Ruhlmann, L.; Lobstein, S.; Maurice Gross, A.; Giraudeau, A. An Electrosynthetic Path toward Pentaporphyrins. *J. Org. Chem.* **1999**, *64*, 1352−1355.
(45) Xu, Y.; Hu, C.; Hu, S. Single-Chain Surfactant Monolayer on Carbon Paste Electrode and its Application for the Studies on the Direct Electron Transfer of Hemoglobin. *Bioelectrochemistry* **2009**, *74*, 254−259.
(46) Kafi, A. K. M.; Naqshabandi, M.; Yusoff, M. M.; Crossley, M. J. Improved Peroxide Biosensor Based on Horseradish Peroxidase/Carbon Nanotube on a Thiol-modified Gold Electrode. *Enzym. Microb. Technol.* **2018**, *113*, 67−74.
(47) Laviron, E. General Expression of the Linear Potential Sweep Voltammogram in the Case of Diffusionless Electrochemical Systems. *J. Electroanal. Chem.* **1979**, *101*, 19−28.
(48) Shi, F.; Zheng, W.; Wang, W.; Hou, F.; Lei, B.; Sun, Z.; Sun, W. Application of Graphene-Copper Sulfide Nanocomposite Modified Electrode for Electrochemistry and Electrocatalysis of Hemoglobin. *Biosens. Bioelectron.* **2015**, *64*, 131−137.
(49) Sun, W.; Dong, L.; Deng, Y.; Yu, J.; Wang, W.; Zhu, Q. Application of N-doped Graphene Modified Carbon Ionic Liquid Electrode for Direct Electrochemistry of Hemoglobin. *Mater. Sci. Eng., C* **2014**, *39*, 86−91.
(50) Sun, W.; Guo, Y.; Ju, X.; Zhang, Y.; Wang, X.; Sun, Z. Direct Electrochemistry of Hemoglobin on Graphene and Titanium Dioxide Nanorods Composite Modified Electrode and its Electrocatalysis. *Biosens. Bioelectron.* **2013**, *42*, 207−213.
(51) Bagheri, H.; Ranjbari, E.; Amiri-Aref, M.; Hajian, A.; Ardakani, Y. H.; Amidi, S. Modified Fractal Iron Oxide Magnetic Nanostructure: A Novel and High Performance Platform for Redox Protein Immobilization, Direct Electrochemistry and Bioelectrocatalysis Application. *Biosens. Bioelectron.* **2016**, *85*, 814−821.
(52) Nie, D.; Liang, Y.; Zhou, T.; Li, X.; Shi, G.; Jin, L. Electrochemistry and Electrocatalytic of Hemoglobin Immobilized on FDU-15-Pt Mesoporous Materials. *Bioelectrochemistry* **2010**, *79*, 248−253.
(53) Sun, W.; Sun, Z.; Zhang, L.; Qi, X.; Li, G.; Wu, J.; Wang, M. Application of Fe_3O_4 Mesoporous Sphere Modified Carbon Ionic Liquid Electrode as Electrochemical Hemoglobin Biosensor. *Colloids Surf., B* **2013**, *101*, 177−182.
(54) Xian, Y.; Xian, Y.; Zhou, L.; Wu, F.; Ling, Y.; Jin, L. Encapsulation Hemoglobin in Ordered Mesoporous Silicas: Influence Factors for Immobilization and Bioelectrochemistry. *Electrochem. Commun.* **2007**, *9*, 142−148.
(55) Wu, Y.; Wang, F.; Lu, K.; Lv, M.; Zhao, Y. Self-assembled Dipeptide-graphene Nanostructures onto an Electrode Surface for Highly Sensitive Amperometric Hydrogen Peroxide Biosensors. *Sens. Actuators, B* **2017**, *244*, 1022−1030.
(56) Guo, Q.; Liu, L.; Zhang, M.; Hou, H.; Song, Y.; Wang, H.; Zhong, B.; Wang, L. Hierarchically Mesostructured Porous TiO_2 Hollow Nanofibers for High Performance Glucose Biosensing. *Biosens. Bioelectron.* **2017**, *92*, 654−660.
(57) Mani, V.; Devadas, B.; Chen, S.-M. Direct Electrochemistry of Glucose Oxidase at Electrochemically Reduced Graphene Oxide-Multiwalled Carbon Nanotubes Hybrid Material Modified Electrode for Glucose Biosensor. *Biosens. Bioelectron.* **2013**, *41*, 309−315.
(58) Wooten, M.; Karra, S.; Zhang, M.; Gorski, W. On the Direct Electron Transfer, Sensing, and Enzyme Activity in the Glucose Oxidase/Carbon Nanotubes System. *Anal. Chem.* **2014**, *86*, 752−757.
(59) Abdelwahab, A. A.; Won, M.-S.; Shim, Y.-B. Direct Electrochemistry of Cholesterol Oxidase Immobilized on a Conducting

DOI: 10.1021/acsami.9b08569
ACS Appl. Mater. Interfaces 2019, 11, 29522−29535

Polymer: Application for a Cholesterol Biosensor. *Electroanalysis* **2010**, *22*, 21−25.
(60) Gholivand, M. B.; Khodadadian, M. Amperometric Cholesterol Biosensor Based on the Direct Electrochemistry of Cholesterol Oxidase and Catalase on a Graphene/Ionic Liquid-modified Glassy Carbon Electrode. *Biosens. Bioelectron.* **2014**, *53*, 472−478.
(61) Deng, C.; Chen, J.; Nie, Z.; Si, S. A sensitive and stable biosensor based on the direct electrochemistry of glucose oxidase assembled layer-by-layer at the multiwall carbon nanotube-modified electrode. *Biosens. Bioelectron.* **2010**, *26*, 213−219.
(62) Luo, Z.; Yuwen, L.; Han, Y.; Tian, J.; Zhu, X.; Weng, L.; Wang, L. Reduced Graphene Oxide/PAMAM-Silver Nanoparticles Nanocomposite Modified Electrode for Direct Electrochemistry of Glucose Oxidase and Glucose Sensing. *Biosens. Bioelectron.* **2012**, *36*, 179−185.
(63) Yu, Y.; Chen, Z.; He, S.; Zhang, B.; Li, X.; Yao, M. Direct Electron Transfer of Glucose Oxidase and Biosensing for Glucose Based on Pdda-Capped Gold Nanoparticle Modified Graphene/Multi-Walled Carbon Nanotubes Electrode. *Biosens. Bioelectron.* **2014**, *52*, 147−152.
(64) Devasenathipathy, R.; Mani, V.; Chen, S.-M.; Huang, S.-T.; Huang, T.-T.; Lin, C.-M.; Hwa, K.-Y.; Chen, T.-Y.; Chen, B.-J. Glucose Biosensor Based on Glucose Oxidase Immobilized at Gold Nanoparticles Decorated Graphene-Carbon Nanotubes. *Enzym. Microb. Technol.* **2015**, *78*, 40−45.
(65) Huang, W.; Ding, S.; Chen, Y.; Hao, W.; Lai, X.; Peng, J.; Tu, J.; Cao, Y.; Li, X. 3D NiO Hollow Sphere/Reduced Graphene Oxide Composite for High-Performance Glucose Biosensor. *Sci. Rep.* **2017**, *7*, 5220.
(66) Jiang, B.; Zhou, K.; Wang, C.; Sun, Q.; Yin, G.; Tai, Z.; Wilson, K.; Zhao, J.; Zhang, L. Label-free Glucose Biosensor Based on Enzymatic Graphene Oxide-Functionalized Tilted Fiber Grating. *Sens. Actuators, B* **2018**, *254*, 1033−1039.
(67) Chen, C.; Xie, Q.; Yang, D.; Xiao, H.; Fu, Y.; Tan, Y.; Yao, S. Recent Advances in Electrochemical Glucose Biosensors: A Review. *RSC Adv.* **2013**, *3*, 4473−4491.
(68) Pinsker, J. E.; Dassau, E. Predictive Low-Glucose Suspend to Prevent Hypoglycemia. *Diabetes Technol. Ther.* **2017**, *19*, 271−276.
(69) Das, P.; Das, M.; Chinnadayyala, S. R.; Singha, I. M.; Goswami, P. Recent Advances on Developing 3rd Generation Enzyme Electrode for Biosensor Applications. *Biosens. Bioelectron.* **2016**, *79*, 386−397.
(70) Patil, A. J.; Muthusamy, E.; Mann, S. Fabrication of Functional Protein-organoclay Lamellar Nanocomposites By Biomolecule-induced Assembly of Exfoliated Aminopropyl-functionalized Magnesium Phyllosilicates. *J. Mater. Chem.* **2005**, *15*, 3838−3843.

DOI: 10.1021/acsami.9b08569
ACS Appl. Mater. Interfaces 2019, 11, 29522−29535